JGR Space Physics

RESEARCH ARTICLE
10.1029/2018JA026243

The Dominant Role of Energetic Ions in Solar Wind Interaction With the Moon

N. Omidi[1], X. Y. Zhou[2], C. T. Russell[2], and V. Angelopoulos[2]

[1]Solana Scientific Inc., Solana Beach, CA, USA, [2]Department of Earth and Space Sciences, UCLA, Los Angeles, CA, USA

Key Points:
- Energetic ions dominate solar wind interaction with the moon
- Lunar tail is populated with energetic ions
- Lunar wake structure consists of compressional and rarefaction fast magnetosonic waves

Correspondence to:
N. Omidi,
omidi@solanasci.com

Citation:
Omidi, N., Zhou, X. Y., Russell, C. T., & Angelopoulos, V. (2019). The dominant role of energetic ions in solar wind interaction with the moon. *Journal of Geophysical Research: Space Physics*, *124*, 3176–3192. https://doi.org/10.1029/2018JA026243

Received 26 OCT 2018
Accepted 20 FEB 2019
Accepted article online 22 FEB 2019
Published online 8 MAY 2019

Abstract We use the results of 3-D electromagnetic hybrid (kinetic ions and fluid electrons) simulations and observations by the Time History of Events and Macroscale Interactions during Substorms (THEMIS) / Acceleration, Reconnection, Turbulence and Electrodynamics of the Moon's Interaction with the Sun (ARTEMIS) spacecraft to investigate the nature of the solar wind interaction with the moon and the resulting wake and tail structure. In the absence of a global magnetic field and an atmosphere at the moon, this interaction is due to the absorption of the solar wind plasma on the dayside and the means by which the resulting cavity in the tail is refilled. To explore this process, we conducted simulations of specific case studies well-monitored by the ARTEMIS spacecraft. Preliminary runs revealed that when the solar wind core plasma is driving the interaction, the results deviate significantly from observations. When the small population of solar wind energetic ions is incorporated in the model, the observations are reproduced much better. Simulations with different density or energy of energetic ions show considerable changes in the results indicating their dominance in establishing the electromagnetic properties of the tail. In contrast, the results show less sensitivity to the solar wind flow speed. Here we conclude that the structure of the interaction region consists of compressional and rarefaction wakes and a central tail region with areas of enhanced and possibly reduced magnetic field level. The compressional wake diverts the flow away from the tail, and its presence is found to be highly time dependent while the rarefaction wake diverts the flow toward the tail and is found to be a semipermanent feature of the lunar interaction region.

1. Introduction

The interaction between the solar wind and the moon is governed by the lack of a lunar atmosphere/ionosphere and a global magnetic field, resulting in the absorption of the solar wind on the dayside and formation of a density cavity in the tail (Lyon et al., 1967; Whang & Ness, 1970). This cavity can extend more than 20 lunar radii (R_m) down the tail before getting refilled by the solar wind (e.g., Clack et al., 2004 ; Denavit, 1979 ; Ogilvie et al., 1996 ; Samir et al., 1983 ; Wang et al., 2011; Zhang et al., 2014). The interplanetary magnetic field (IMF) penetrates the moon with little or no change; however, behind the moon, the field is enhanced in the central tail region and reduced on the flanks/wakes (Colburn et al., 1967; Ness et al., 1968; Sonett, 1982). A number of studies in the past have examined the nature of the lunar current system that forms due to solar wind interaction (Colburn et al., 1967; Fatemi et al., 2013; Halekas et al., 2005; Holmström et al., 2012; Michel, 1968; Owen et al., 1996). In regard to the nature of the lunar wake, previous studies have indicated the formation of fast magnetosonic rarefaction wakes where density and magnetic field fall below solar wind levels (e.g., Fatemi et al., 2013 ; Holmström et al., 2012 ; Xie et al., 2012). On the other hand, Zhang et al. (2016) have also suggested the formation of Alfvén wings in the wake.

In this study, we take the approach of comparing the results of 3-D hybrid (kinetic ions and fluid electrons) simulations to specific lunar tail crossings in order to examine and improve our understanding of the solar wind interaction with the moon under steady solar wind conditions. In section 2, we describe a lunar tail crossing by the THEMIS/ARTEMIS spacecraft (Angelopoulos, 2008, 2011) during a period of steady solar wind conditions used to compare with the simulation results. Using the solar wind conditions during this event as input for a hybrid run, we show that the results are far different from the spacecraft observations. This shortcoming of the model is addressed by examining the effects of including the observed high energy ions in the solar wind in the hybrid model in section 3. Previous studies (Dhanya et al., 2013; Nishino et al., 2013) have examined the access of energetic ions to the lunar tail during periods of radial IMF where the flow and the magnetic field are aligned. Here we show that

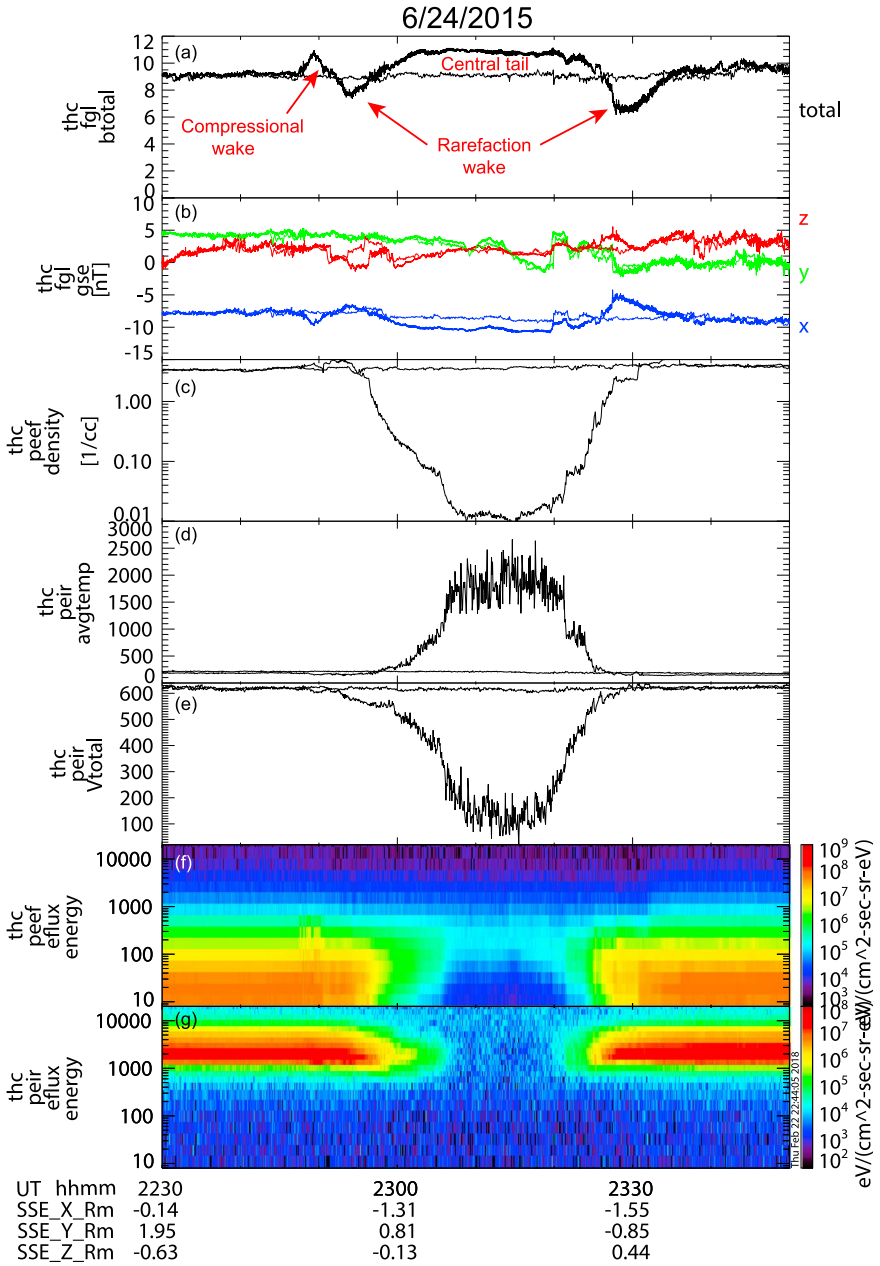

Figure 1. THC crossing of the lunar tail on 24 June 2015. (a) and (b) show the total magnetic field and its components, respectively. (c)–(e) correspond to density, temperature, and velocity with (f) and (g) showing electron and ion energy spectrum. THB observations in the solar wind are shown with thinner lines.

inclusion of a small population of energetic ions in the simulations leads to a dramatic change in the results bringing them much closer to spacecraft observations. By changing the density or energy of the energetic ions, we demonstrate the dominant role of these ions in establishing the electromagnetic properties of the lunar tail. In section 4, we examine the sensitivity of the simulation results to solar wind flow velocity and IMF direction and discuss the general structure of the lunar interaction region. The significance of the IMF direction in determining the nature of the interaction region has been discussed in previous studies (e.g., Colburn et al., 1971; Fatemi et al., 2013; Holmström et al., 2012; Sibeck et al., 2011; Whang, 1968; Xie et al., 2012). A summary and the conclusions of the study are presented in section 5.

Table 1
Hybrid Simulation Run

Run	Cone angle (°)	N-SW (%)	V-SW (km/s)	T-Sw (eV)	N-EI (%)	V-EI (km/s)	T-EI (eV)
0	30	100	610	22	0		
1	30	99	610	22	1	610	230
2	30	99	610	22	1	925	926
3	30	97	610	22	3	1134	926
4	30	99	505	22	1	610	230
5	0	99	610	22	1	610	230
6	60	99	610	22	1	610	230

Note. Columns from left to right show the run number, cone angle, cold solar wind relative density, cold solar wind velocity, cold solar wind temperature, energetic ions relative density, velocity of the energetic ions, and temperature of the energetic ions.

2. Hybrid Simulation of a Lunar Tail Crossing

In order to understand the steady-state structure of the lunar interaction region, it is necessary to focus on periods of relatively steady solar wind conditions. Figure 1 shows ARTEMIS observations of the lunar tail on 24 June 2015 when solar wind conditions are relatively steady. Figures 1a and 1b show the total magnetic field and the three components of the field, respectively, while Figures 1c–1e show the electron (also representing ion) density, ion temperature, and velocity measured by Electrostatic Analyzer (ESA) on THEMIS-C. We note that due to instrument limitations (ESA instrument on THEMIS does not measure the core solar wind protons with the required resolution), the solar wind temperature of ~200 eV in Figure 1 is an overestimate. Based on time-shifted measurements by the Wind spacecraft, we use a temperature of 22 eV. The field components are in the Geocentric solar ecliptic (GSE) coordinate system with

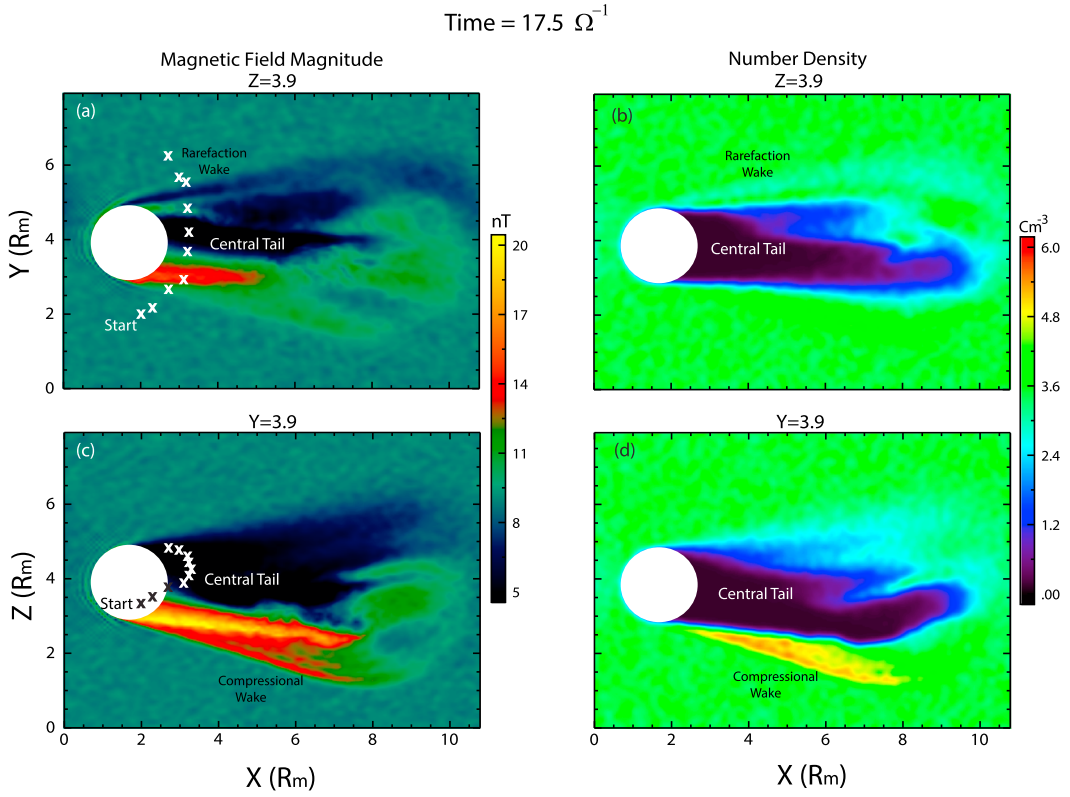

Figure 2. Magnetic field and density from run 0 in (a, b) X-Y and (c, d) X-Z planes. THC trajectory is shown using "x" sign.

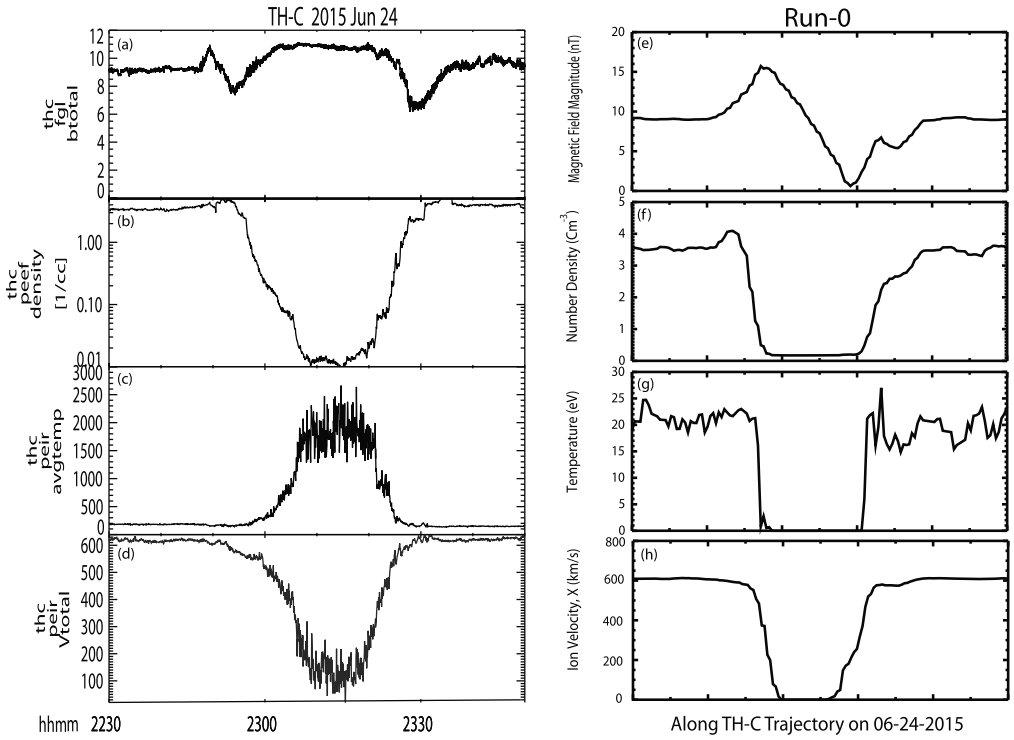

Figure 3. (a)–(d) show total magnetic field, density, temperature, and velocity measured by THC. (e)–(h) correspond to results of run 0 along THC trajectory.

X pointing toward the Sun, Z points north, and Y completes a right-handed coordinate system. Electron and ion energy spectra are shown in Figures 1f and 1g. THEMIS-B observations in the solar wind are shown with thinner lines. As can be seen, the IMF field strength in the solar wind before and after the tail crossing is steady at a value of ~9 nT with B_x as the dominant component and also remaining steady. This corresponds to an IMF cone angle (with respect to the solar wind velocity) of ~30°. On the other hand, the weaker B_y and B_z components do indicate some variation with time in the solar wind. Also, solar wind density, velocity, and temperature remain steady at 3.5 cm^{-3}, 610 km/s, and 22 eV, respectively. The ARTEMIS observations are processed using SPEDAS 3.1, a grass-roots software development platform supported by National Aeronautics and Space Administration (NASA) Heliophysics (Angelopoulos et al., 2019).

The magnetic signatures of the tail crossing consist of enhancement above IMF level identified as a compressional wake, drops below solar wind values associated with a rarefaction wake and a central tail region with magnetic field levels above IMF value. Both the compressional and rarefaction wakes are associated with correlated changes in magnetic field and density and as such fall on the fast magnetosonic branch. However, a major distinction is that the compressional wake diverts the solar wind flow away from the tail (similar to a fast shock), while the rarefaction wake results in flow diversion toward the tail. Therefore, their role in the structure and dynamics of the lunar tail is considerably different. We note that the changes in B_x are similar to those observed in the total magnetic field as expected. During the tail crossing, plasma density drops to values slightly above 0.01 cm^{-3}, while ion temperature rises to ~2,000 eV and ion velocity decreases to below 100 km/s. We note that the plasma moments are computed automatically onboard the spacecraft as described in McFadden, Carlson, Larson, Bonnell et al. (2008) and McFadden, Carlson, Larson, Ludlam, et al. (2008).

Using the solar wind conditions observed during this event as input, we conducted a hybrid simulation run named run 0 in Table 1. This model has been used in the past to investigate the interaction of Saturn's corotating plasma with Enceladus (Omidi et al., 2012) and solar wind interaction with Venus (Omidi et al., 2017). The simulation box consists of 150 × 150 × 100 cells in the X, Y, and Z directions with the

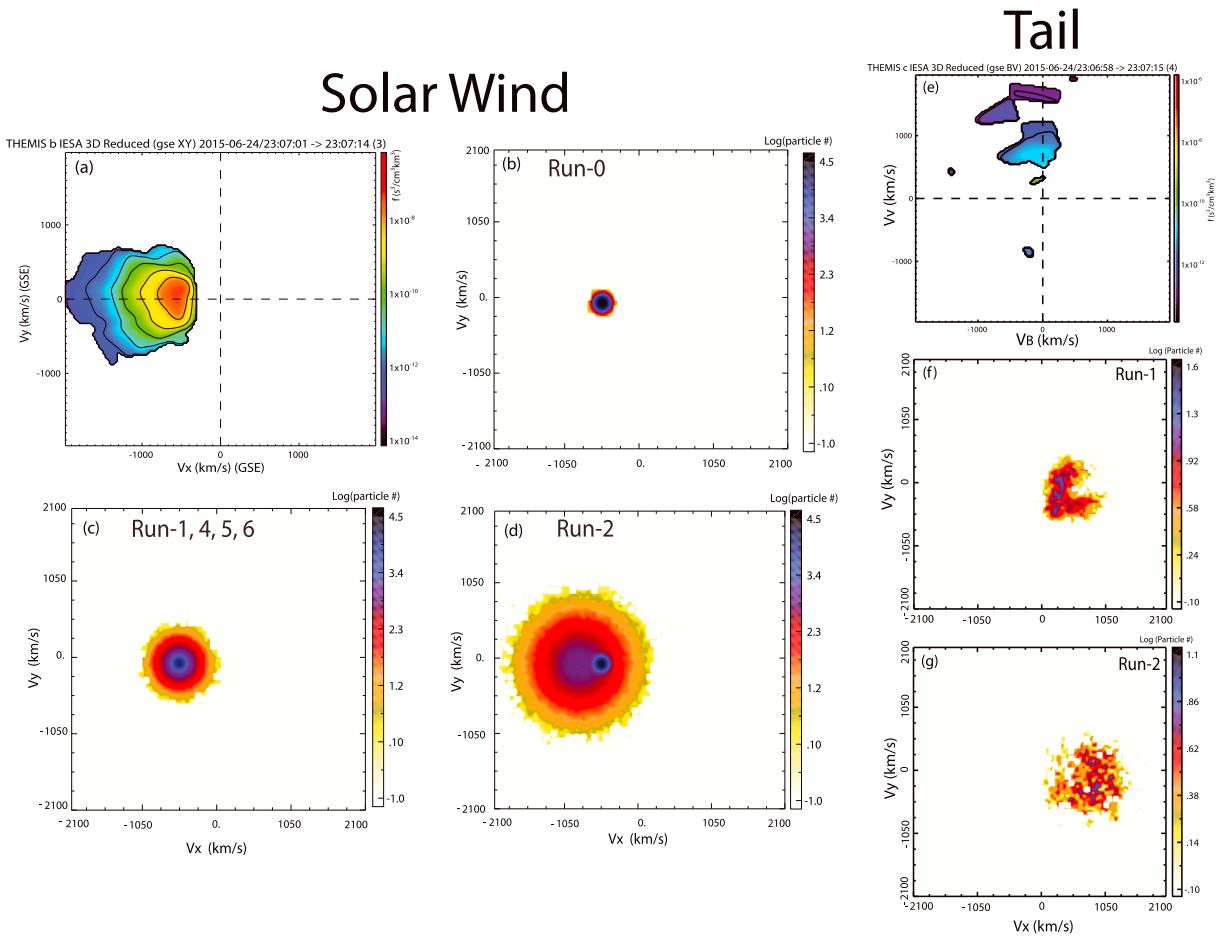

Figure 4. (a)–(d) show the measured and simulated ion velocity distribution functions in the solar wind. (e)–(g) show measured and simulated ion distribution functions in the lunar tail.

simulation X axis in the solar wind flow direction, Z points to north, and Y completes a right-handed system. Note that the GSE X and Y axes are directed in the opposite orientations as compared to the simulation X and Y axes, while the Z direction is the same for both coordinate systems. Given the small and time-varying value of B_Z in Figure 1, we assume IMF initially lies in the X-Y plane with a cone angle of 30°. Except for run 0, the simulation box is 150 × 150 × 100 proton skin depth (c/ω_p) corresponding to 10.7 × 10.7 × 7.1 lunar radii (R_m) and uses a total of 4×10^7 particles. Solar wind plasma is continuously injected from the X = 0 boundary and allowed to leave the system from the remaining boundaries. The center of the moon is placed at X = 1.8, Y = 7.1, and Z = 3.6 R_m, and it is treated as a plasma absorbing body so that upon hitting it the particle is removed from the simulation box. Floating boundary conditions are used so that the electromagnetic fields on the lunar boundary can change with time and are not fixed to any specific values. We note that in run 0, the simulation box is 150 × 110 × 110 proton skin depth with moon centered at Y = 3.9.

Figure 2 shows the total magnetic field strength and density in the X-Y and the X-Z planes from run 0. Figures 2a and 2b show the presence of a rarefaction wake associated with magnetic field and density below solar wind values. Figure 2a also shows a central tail region consisting of areas of reduced and enhanced magnetic field strength. A similar central tail region can also be seen in the X-Z plane which also shows a compressional wake associated with enhanced magnetic field and density. In order to compare the results of this run to spacecraft observations, we fly a simulated spacecraft through the simulation box using the trajectory by THC. Figure 3 compares the observations by THC to those associated with run 0. Figures 3a and 3e compare the measured and simulated magnetic field strength which show little

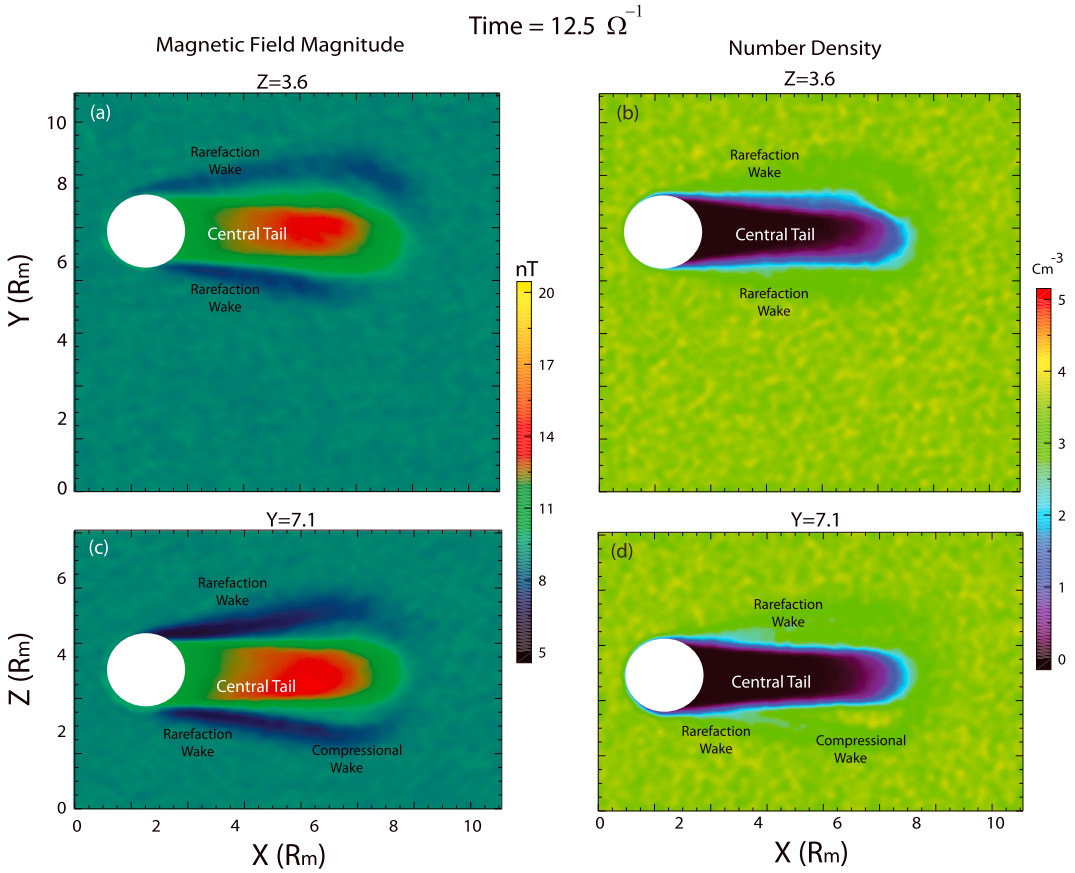

Figure 5. Magnetic field and density from run 1 in (a, b) X-Y and (c, d) X-Z planes.

resemblance to each other. The measured and simulated densities in Figures 3b and 3f show some resemblance in that they both show an enhancement associated with the compressional wake before entering the cavity region in the central tail and a reduction in density associated with the rarefaction wake prior to reentering the solar wind. Within the cavity, the simulated density is at a constant level of 5% of solar wind value (0.17 cm^{-3}) used as a minimum in the regions where no ions are present. The use of this minimum density is in order to avoid the Alfvén velocity in that region approaching infinity. It is however the case that no ions from the solar wind reach the central tail region near the moon, and as a result, the simulated ion temperature and velocity in the central tail region are zero. Based on the results in Figure 3, we conclude that comparison between the simulation results and observations show little agreement between the two.

3. The Impact of Energetic Ions

A telling difference between the observations and the results of run 0 in Figure 3 is that no ions are found in the central tail region of the model, while in reality, a small population of plasma is present in that region. This suggests that the simulation does not fully represent the plasma configuration in the solar wind. In particular, given that ions with energies of approximately greater than hundreds of electronvolts have gyro-radii comparable or larger than lunar radii, their interaction with the moon would be different than lower energy ions. Therefore, if such ions are present in the solar wind, they need to be accounted for in the model. Figure 4a shows a typical ion velocity distribution function in the solar wind on 24 June 2015 in GSE coordinate system, while Figure 4b shows the ion velocity distribution function in the solar wind in run 0. An apparent difference between the distributions in Figures 4a and 4b is that in the latter, the high energy ions have been left out. In order to bring the simulated solar wind closer to the observations, it is necessary to include a second population of energetic ions in the model as described below.

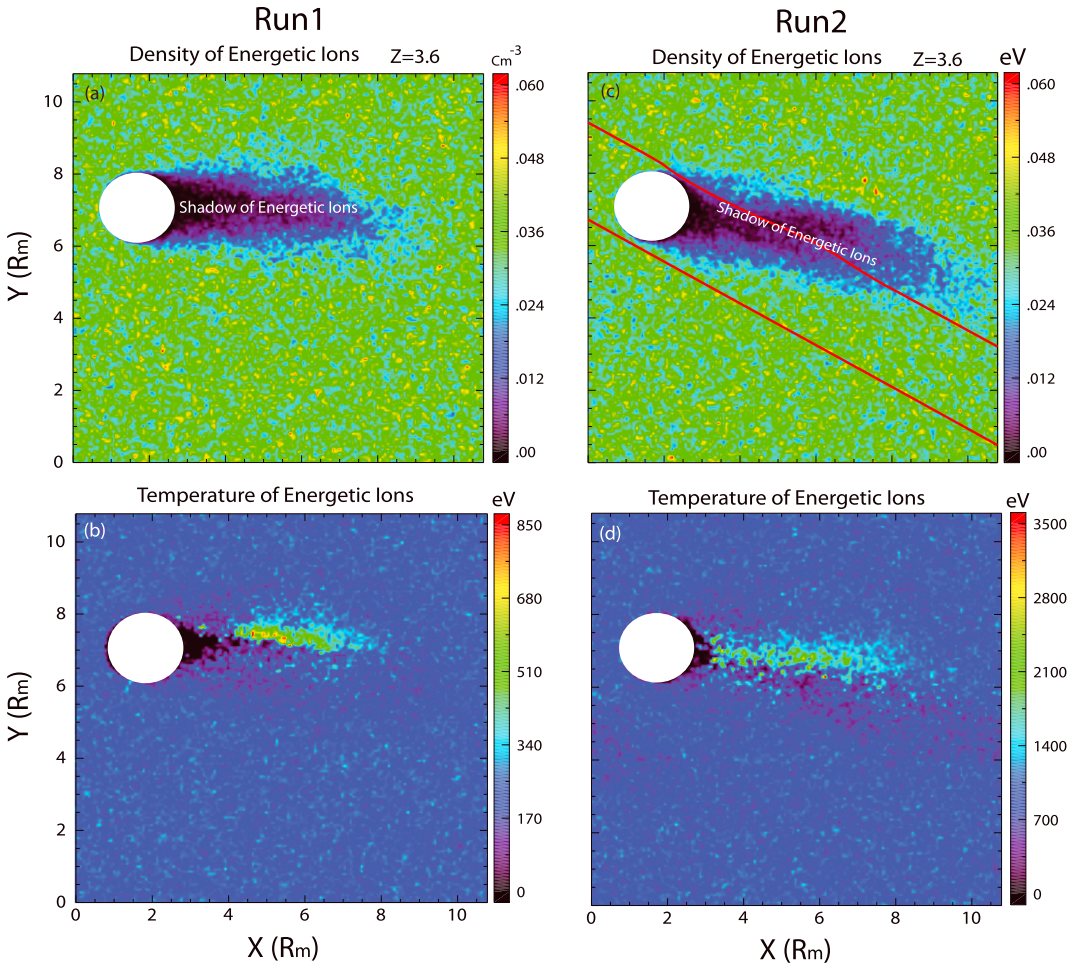

Figure 6. Density and temperature of energetic ions from Runs 1 and 2 in X-Y plane.

Table 1 shows the plasma parameters used in run 1 which includes two populations of ions. The cold solar wind constitutes 99% of ions and is represented by a Maxwellian distribution function with flow speed of 610 km/s and temperature of 22 eV. The remaining 1% energetic ions are modeled as another Maxwellian distribution function with the flow speed of 610 km/s and temperature of 230 eV. We have also examined the effects of increasing the flow speed and temperature of energetic ions to 925 km/s and 926 eV, respectively, in run 2. Figures 4c and 4d show the velocity distribution function of the solar wind ions in runs 1 and 2, respectively. In the following, we describe the results of these two runs.

Figure 5 shows the magnetic field and total (cold and energetic ions) density from run 1 which illustrates the presence of a rarefaction wake in X-Y and X-Z planes, while a compressional wake is observed in the X-Z plane. The central tail region is primarily associated with the enhancement of the magnetic field. Figure 6 shows the density and temperature of the energetic ions in the X-Y plane for Runs 1 and 2. Also shown are two magnetic field lines drawn in panel (c). It is evident from this figure that unlike the cold solar wind protons, both the density and temperature of the energetic ions in the central tail region are finite with the later above its value in the solar wind. Also evident in Figure 6a,c is the presence of a shadow of energetic ions behind the moon which depending on the properties of the energetic ions is flow aligned (6a) or closer to field aligned (6c). The formation of a nearly field aligned shadow clearly demonstrates the notion that in reality, ions undergo a combination of motion along the magnetic field and gyration around it and that when the gyro-radius is comparable or larger than the lunar (obstacle) radius dayside absorption by the moon occurs differently allowing for their access to the tail. Note that, for low

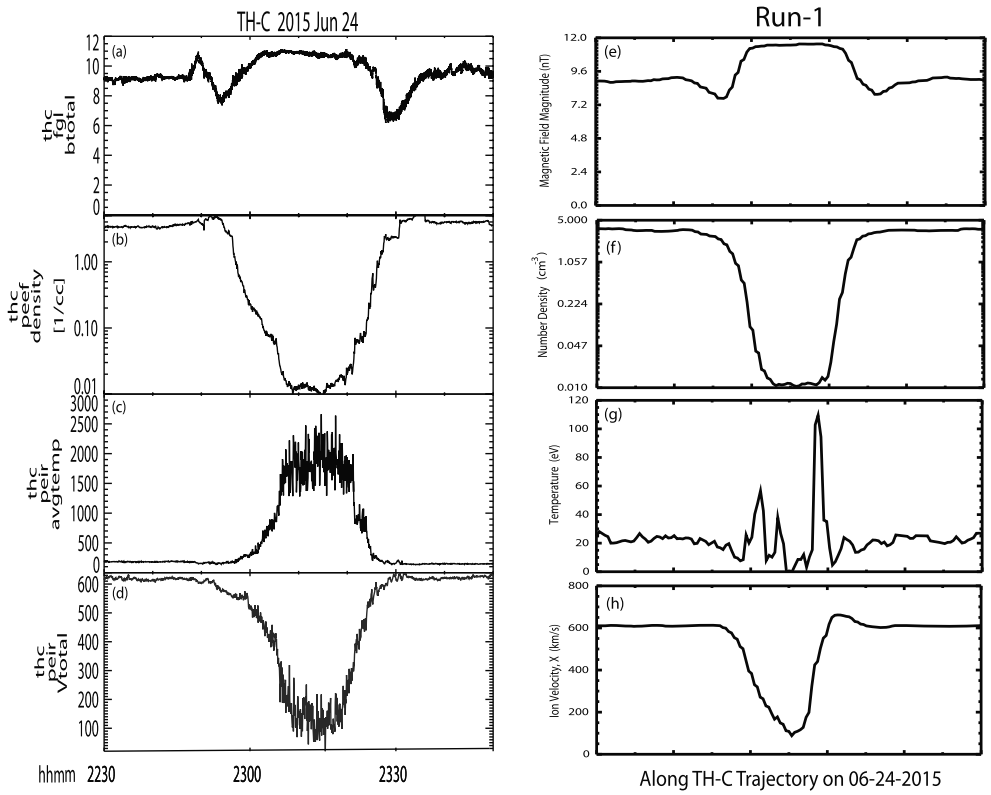

Figure 7. (a)–(d) show total magnetic field, density, temperature, and velocity measured by THC. (e)–(h) correspond to results of run 1 along THC trajectory.

energy ions with much smaller gyro-radius, one can view their motion to be essentially along the flow direction.

Figure 7 is similar to Figure 4 and compares the results of run 1 along THC trajectory to spacecraft observations. Comparing the magnetic field strength, it is evident that except for the absence of a strong compressional wake in the simulation data, the remaining features namely the inbound and outbound rarefaction wakes and the central tail region look similar. Instead of a strong compressional wake, a weak compressional wake is present in panel (e). The reason for this difference is discussed in the next section. The presence of energetic ions in run 1 brings the plasma measurements in the simulated tail closer to spacecraft observations with the minimum densities around ~0.01 cm^{-3} and enhanced temperatures in both cases albeit the ones in THC observations are higher in value. Note that while Figure 7d shows the total observed velocity, Figure 7h shows the simulated V_x.

To understand the cause of the observed and simulated temperature increases in the central tail region and the differences in their maximum values (~2,000 vs. 120 eV), it is necessary to examine the corresponding ion velocity distribution functions. Figure 4e shows a typical ion velocity distribution function measured by THC in the central tail region with V_B and V_V corresponding to velocity along the magnetic field and the direction of ExB velocity, respectively. It is evident that this distribution function is far from a thermal (Maxwellian) configuration, and as such, the calculated second moment of the distribution does not physically signify a true temperature. Therefore, no heating or energization mechanism is needed to explain the apparent increase in the observed temperature. Another way of stating this point would be that the apparent increase in the calculated temperature is associated with the absorption and removal of the core solar wind protons from the distribution functions in the tail. Figures 4f and 4g show the velocity distribution functions of ions in the central tail region in runs 1 and 2, respectively. As with the observed distribution function, they are also nonthermal in nature, and the calculated second moments do not represent temperature in a physically meaningful way that corresponds to thermal distribution functions (e.g., Maxwellian). Comparing Figures 4c to 4f and 4d to 4g shows that velocities observed in the tail region fall within those present in

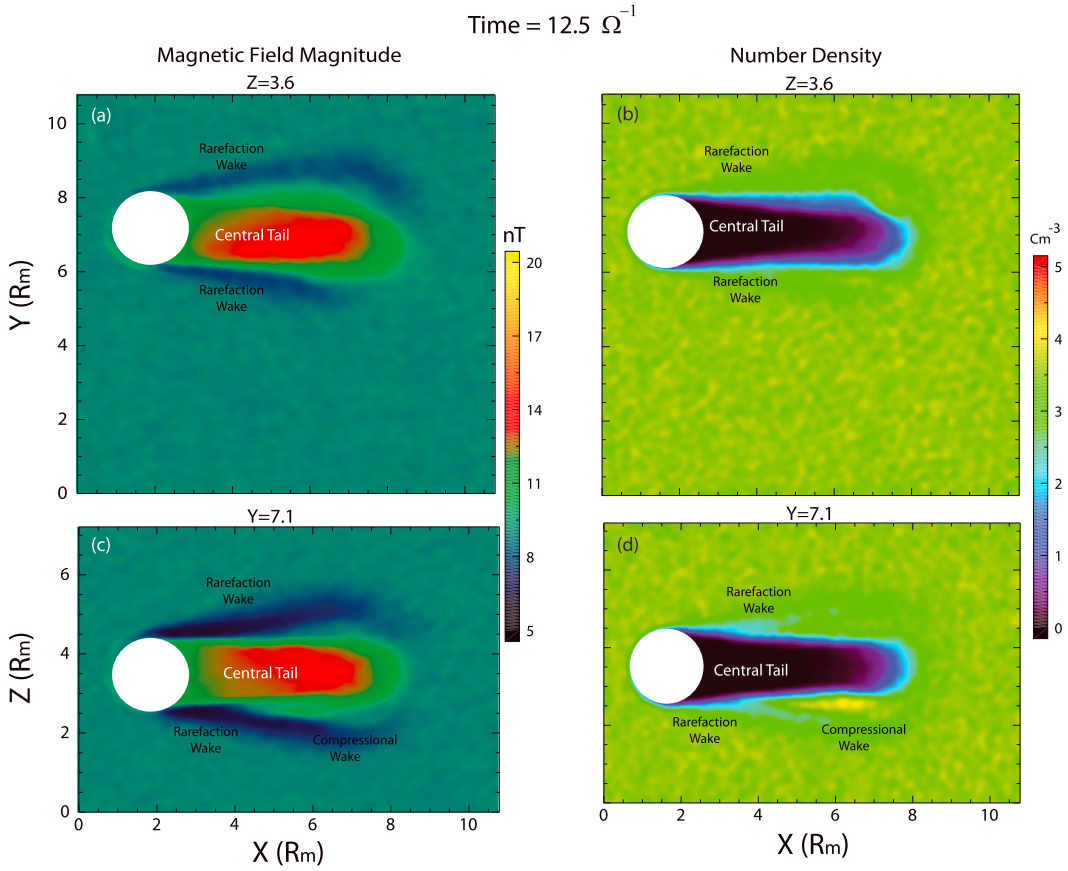

Figure 8. Magnetic field and density from run 2 in (a, b) X-Y and (c, d) X-Z planes.

the solar wind, and therefore, no energization process is needed to explain their presence. In short, the apparent increases in the observed and simulated ion temperatures are the consequence of the access of energetic ions to the central tail region and the resulting nonthermal distribution function that is formed.

Figure 8 shows the total magnetic field strength and density from run 2 and shows stronger field strength in the central tail region as compared to run 1 indicating the significance of the energetic ions. To further explore the role of energetic ions in determining the properties of the lunar tail, we performed run 3 which is similar to run 2 except that the density of the energetic ions is increased to 3% of the total and velocity is increased to 1134 km/s. Figure 9 shows the density and magnetic field from this run and demonstrates major changes in the lunar tail. A comparison between Figure 9 and 5 shows that in run 3, the maximum field strength reached in the central tail region is larger and also regions of reduced magnetic field occupy a larger portion of the tail region. These results demonstrate that by virtue of being the only population of ions to reach the central tail region, the energetic ions play a dominant role in determining the electromagnetic properties of the lunar tail.

4. Sensitivity to Other Solar Wind Parameters

Although a detailed parametric research of the lunar interaction region is beyond the scope of this study, it is instructive to examine the sensitivity of the simulation results to the solar wind velocity and the IMF direction. Accordingly, run 4 is similar to run 1 except that the flow speed of the cold ions is reduced from 610 to 505 km/s which corresponds to reducing the Alfvén Mach number from 5.8 to 4.8. The results are shown in Figure 10 which when compared to Figure 5 shows a very similar structure except that the length of the tail is not as long. Given that the two figures correspond to the same time in the simulation, the shorter length of the tail when the flow speed is reduced is understandable. Except for this difference however, the results of

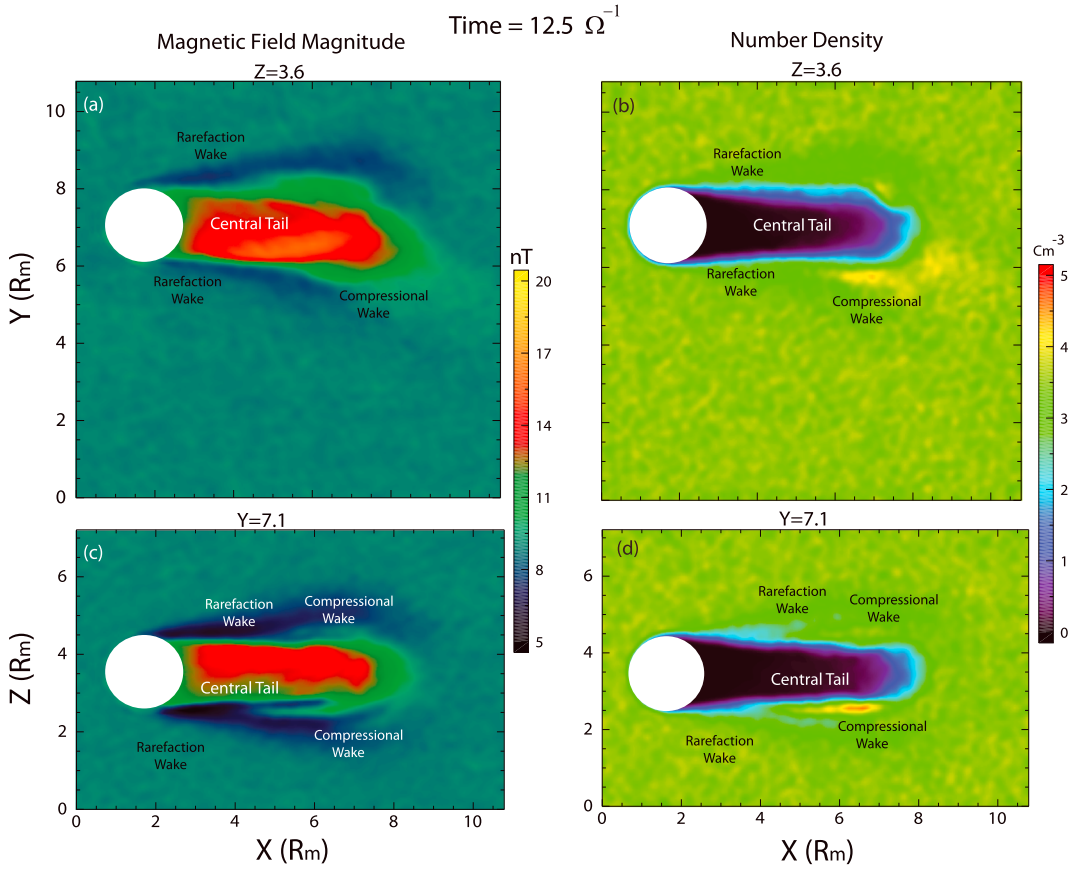

Figure 9. Magnetic field and density from run-3 in (a, b) X-Y and (c, d) X-Z planes.

runs 1 and 4 are very similar, indicating very low sensitivity to the flow speed of the cold ions and further establishing the dominant role of the energetic ions.

Run 5 is similar to run 1 except that the IMF cone angle is 0° with the results illustrated in Figures 11a and 11b. As can be seen, the interaction region consists of a region of enhanced magnetic field in the central tail and a rarefaction wake that surrounds it. This structure is similar to that shown by Holmström et al. (2012) and Fatemi et al. (2013). No compressional wakes are formed in this run. In contrast, Figures 11c and 11d correspond to run 6 where the IMF cone angle is 60° and show a more asymmetric rarefaction wake with a much stronger wake in the X-Z plane. Note the difference in the scale of the magnetic field strength in Run-6 indicating a weaker enhancement of the field in the central tail region as compared to Run-5.

Figure 12 compares the total magnetic field strength from runs 1 to 6 along the THC trajectory (note the differences in scale). The field profile in Figure 12a corresponds to run 1 and most closely resembles the observations, while Figures 12b and 12c show profiles from runs 2 and 3 and clearly illustrate deviations from the observations in maximum field strength in the central tail region. Figure 12d corresponds to run 4 and shows considerable similarity to Figure 12a, indicating the reduced sensitivity of the lunar tail structure to the cold solar wind Mach number. The magnetic field structure shown in Figure 12e indicates central tail field strengths larger than observations, although the field profile is similar. The profile obtained in run 6 shown in Figure 12f is considerably different from the observations, indicating the significance of the cone angle in determining the lunar tail structure.

Although the field profiles in Figure 12 are along the THC trajectory, they correspond to a single time in the simulation and therefore, question arises regarding the variability of these profiles in time. Figure 13 addresses this question by showing profiles of the magnetic field from each run at 25 different times

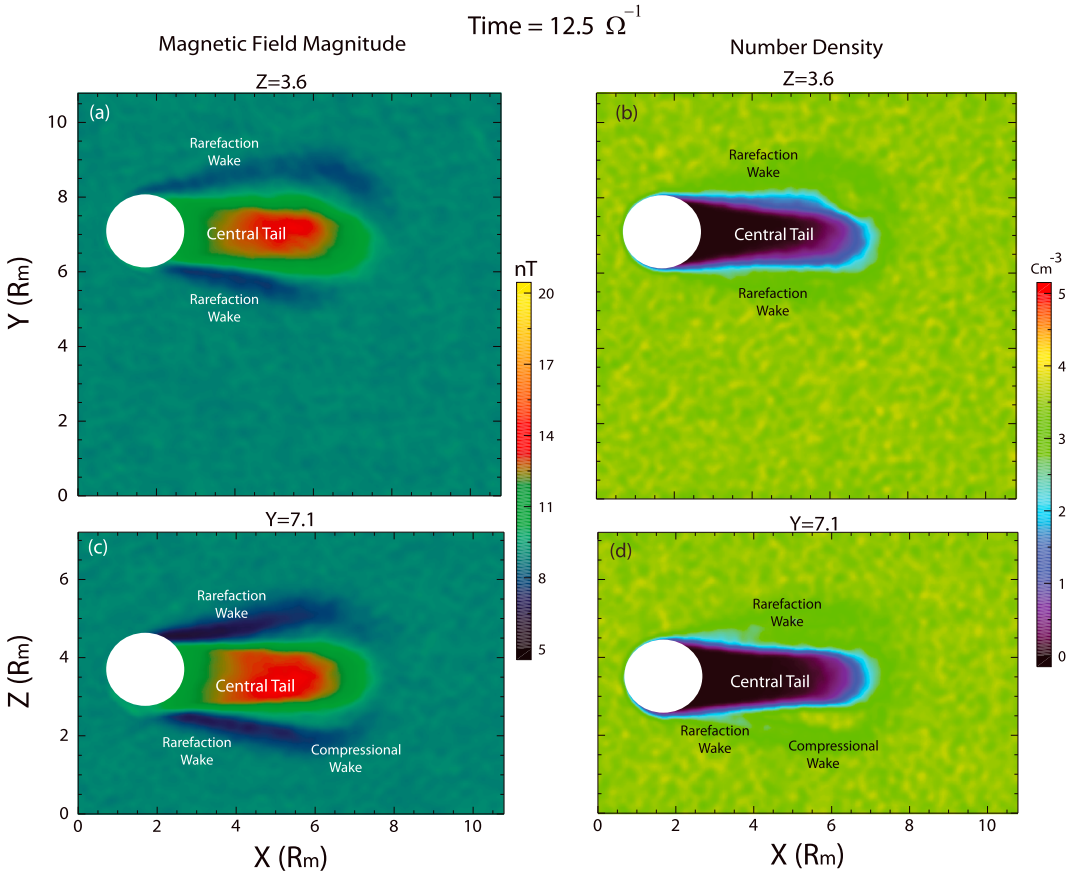

Figure 10. Magnetic field and density from run 4 in (a, b) X-Y and (c, d) X-Z planes.

between 6.25 and 12.5 Ω^{-1}. Figure 13a corresponds to run 1 and shows very little change in the field profile with time, while runs 2 and 3 show more dependency on time. Figure 13d shows that run 4 has a time profile very similar to run 1 consistent with the notion that the results are not very sensitive to changes in flow speed. Figure 13e indicates a truly time stationary solution with no perceptible change in field profile when the IMF is along the solar wind velocity.

The fact that run 1 does a good job in reproducing THC observations is due to the fact that as shown in Figure 13, the tail structure in this run is nearly time stationary. If on the other hand, the observed IMF cone angle had been 60° where the tail structure shows more time variability, it would have required some level of luck for the observed and simulated tail structures to match as closely. Examination of the simulation results show that while nearly time stationary solutions for the rarefaction wake and the central tail region are possible, the compressional wake is highly time and also location dependent. This provides a possible explanation for why run 1 does not show the presence of a strong compressional wake along the THC trajectory despite a good agreement with other parts of the tail structure. In the following, we elaborate further on this possibility.

Figure 14a shows the total magnetic field strength in a cross section of the lunar tail in the Y-Z plane. It is evident that the rarefaction wake represented in dark blue and purple colors nearly surround the lunar tail, while a region of enhanced magnetic field protrudes from the central tail region which corresponds to the compressional wake. Figures 14b and 14c show the density and magnetic field strength along the dashed line labeled "L" and show a profile that includes the compressional wake and is similar to that observed by THC. Figures 14d–14g show the lunar cross section in the Y-Z plane at X = 6.1 at four times during the run and demonstrate that the compressional wake is not only relatively localized, its location is highly variable with time due to the internal dynamics of the tail. In contrast, while the rarefaction wake shows some time

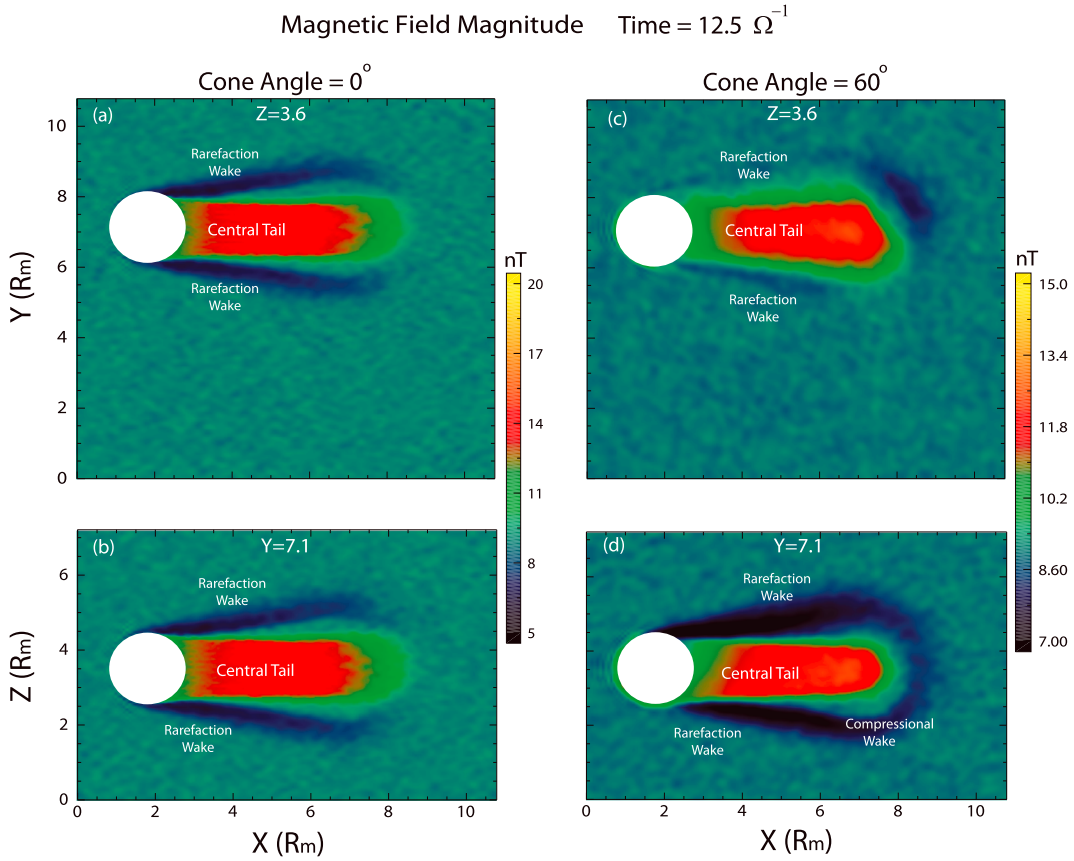

Figure 11. Magnetic field from runs 5 and 6 in (a, b) X-Y and (c, d) X-Z planes.

dependency, it remains a semipermanent feature of the tail. We believe this contrast provides the explanation for run 1 not showing a strong compressional wake along THC trajectory.

If indeed the time dependency of the compressional wake is the reason for its absence in run 1 along the THC trajectory, then by the same argument, there must be observations of the lunar tail that do not include the compressional wake. A preliminary search of the lunar tail crossings show ample examples of signatures without the compressional wake two of which are shown in Figure 15. Figure 15a shows the total magnetic field strength measured by THB (red) and THC (blue) on 12 August 2016 with the former spacecraft in the solar wind and the latter crossing the lunar tail. A comparison between the two magnetic field profiles clearly illustrates the presence of inbound and outbound rarefaction wakes and the central tail region with field strength above solar wind levels. Also evident is the absence of the compressional wake which supports the notion that this wake is time dependent and not a semipermanent feature of the tail structure. Note that the cone angle in this case is similar to the 24 June 2015 crossing, namely, ~30°.

Another clear evidence for the time-dependent nature of the compressional wake is provided in the THB and THC crossings of the lunar tail on 27 August 2016 shown in Figures 15b and 15c. Figure 15b shows THB crossing of the lunar tail, while THC is in the solar wind. It shows the presence of a compressional wake prior to encountering of the inbound rarefaction wake followed by the central tail and the outbound rarefaction wake. Figure 15c corresponds to 3 hr later when THB is in the solar wind and THC crosses the lunar tail. By this time, THC encounters the inbound and outbound rarefaction wakes along with the central tail region without encountering the compressional wake observed earlier by THB even though the cone angle has not changed. This again provides support for the local and time-dependent nature of the compressional wake that in contrast to the rarefaction wake is not a semipermanent feature of the lunar tail structure.

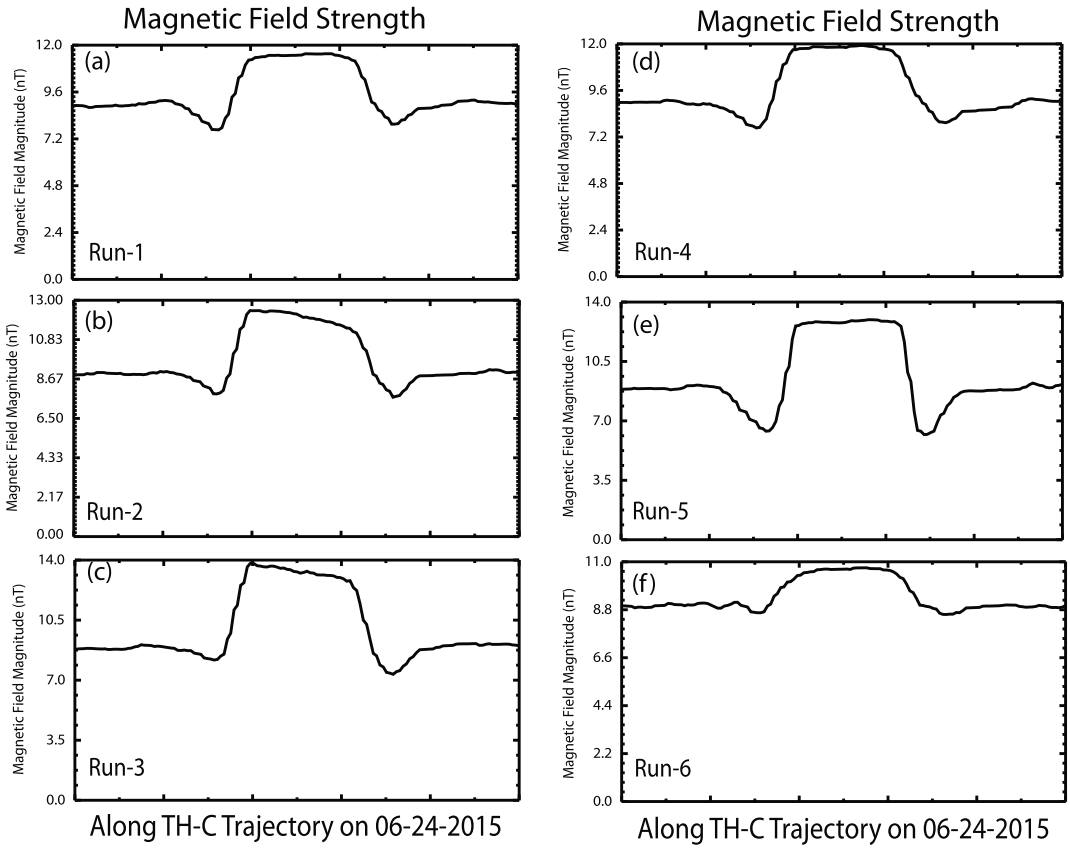

Figure 12. Magnetic field profile along THC trajectory from runs 1 to 6 in panels (a) to (f), respectively.

5. Summary and Conclusions

In this study we use ARTEMIS observations of the lunar tail and 3-D hybrid simulations of solar wind interaction with the moon to investigate and understand the nature of the resulting structure. In the absence of a global magnetic field and an ionosphere, the lunar surface is directly exposed to the solar wind resulting in its absorption on the dayside. This also results in the formation of a density cavity in the tail region, the filling of which determines the overall structure of the interaction region. In particular the formation of lunar wakes and the electromagnetic properties of the central tail region are in response to this plasma cavity and how it gets refilled with distance behind the moon.

Given our desire to understand the quasi-stationary structure of the lunar tail, we chose the spacecraft crossing on 24 June 2015 with nearly steady solar wind conditions to compare with the results of hybrid simulations using input parameters from the observations. In particular, the solar wind density, velocity, and temperature along with the IMF strength and direction measured by spacecraft were used as input in run 0 to generate a simulated tail structure to be compared with the observations. The results show poor agreement between the two indicating a missing element in the model. To address this shortcoming, we examined the impacts of energetic ions present in the solar wind and show that their inclusion in the simulations brings the results much closer to spacecraft observations. By virtue of their much larger gyro-radii, the energetic ions in the solar wind interact with the moon quite differently than cold ions whose motion is to a good degree visualized as being along the flow direction. In the case of the energetic ions, a more accurate picture must take into account motion along the magnetic field and gyration about it at times resulting in the formation of a nearly field-aligned shadow of energetic ions in the tail and more importantly, the access of these ions to the main density cavity formed along the flow direction.

By performing simulation runs with different densities, velocities, or temperatures for the energetic ions, we find considerable changes in the electromagnetic properties of the lunar tail, demonstrating the dominance

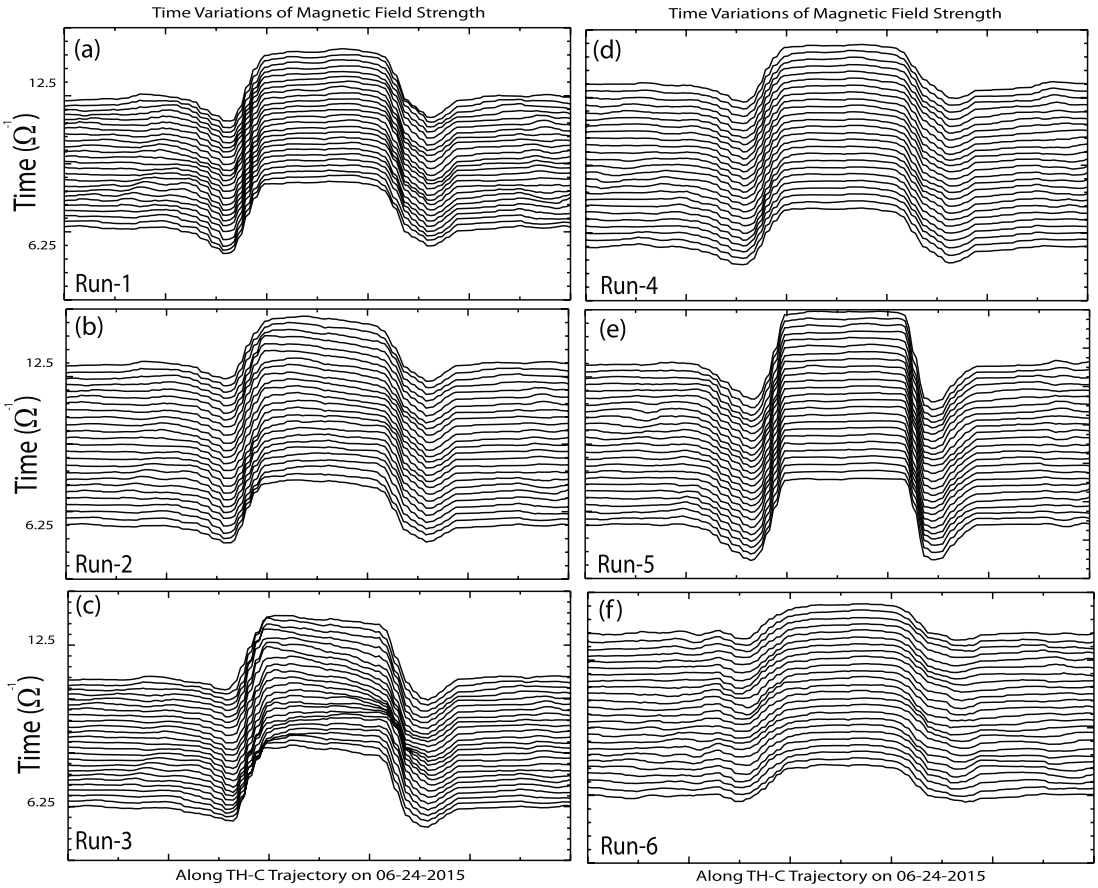

Figure 13. Time variations of the magnetic field profile along THC trajectory from runs 1 to 6 in panels (a) to (f), respectively.

of these ions in determining the nature of the interaction. Although the energetic ions constitute a small minority of solar wind ions, their dominance is not surprising because they are the only population with access to the near-tail region. In a hybrid run with the velocity of the cold solar wind reduced by more than 100 km/s, we find the nature of the interaction region to remain the same demonstrating the reduced sensitivity of the interaction region to the bulk speed of this plasma.

The results of this study indicate that the structure of the lunar tail consists of two types of wakes and a central tail region with the former consisting of rarefaction and compressional components both on the fast magnetosonic branch. The rarefaction wake is associated with correlated decreases in density and magnetic field implying pressure lower than solar wind. As a result, solar wind flow is deflected toward the lunar tail. On the other hand, the compressional wake consists of correlated increases in density and magnetic field and is associated with pressure above solar wind level and pushes the flow away from the tail. The magnetic properties of the central tail region vary with changes in the properties of the energetic ions and also the direction of the IMF and in general correspond to areas of enhanced and possibly reduced field strength.

Both spacecraft observations and hybrid simulations with energetic ions show that while the densities drop within the tail, ion temperature seemingly increases raising questions regarding the underlying mechanisms. Examination of both observed and simulated ion velocity distribution functions in the lunar tail shows that they are highly nonthermal (non-Maxwellian), and therefore, the calculated second moments do not indicate true temperature. As such, the apparent increase in ion temperature is a direct result of the access of energetic ions to this region, and no process for heating of ions is needed.

Comparison of the simulation results with spacecraft observations on 24 June 2015 shows an apparent disagreement in regard to the compressional wake which is much weaker along THC trajectory in the simulations, although it is present in other regions of the simulations. Examination of the

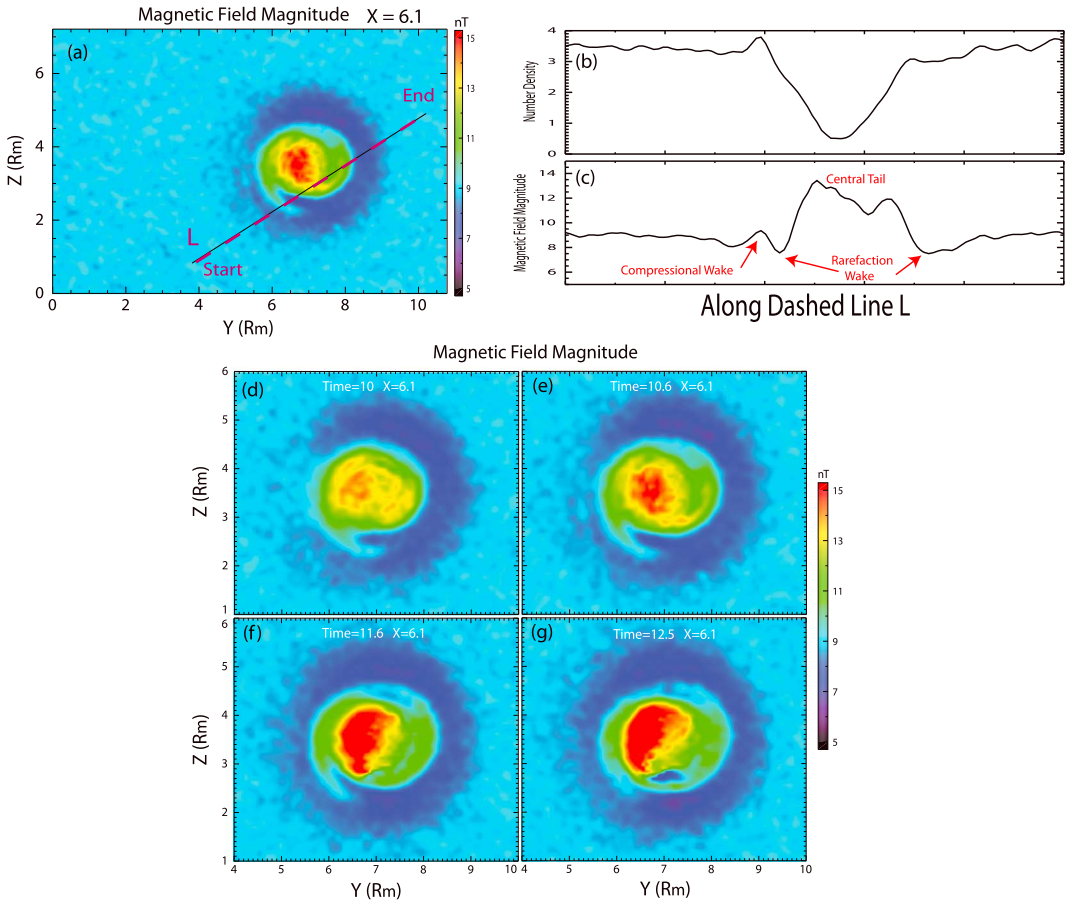

Figure 14. (a) Cross section of the lunar tail in the Y-Z plane shows magnetic field strength. (b) and (c) show the variations of density and magnetic field along line L in (a). (d)–(g) show magnetic field strength at four different times during the run.

compressional wake in the simulations shows that they are highly time dependent, and while they may be present in some parts of the interaction region, they are absent in other parts of the tail. This provides a possible explanation for the disagreement between the observations on 24 June 2015 and simulations. If as expected, the compressional wake is highly time dependent then there should be evidence of lunar tail crossings that do not include the compressional wake. Here we show two examples on 12 and 27 August 2016 that confirm our expectations. On 12 August 2016, the lunar crossing consists of inbound and outbound rarefaction wakes and the central tail region with enhanced magnetic field strength, but no compressional wake even though the cone angle is similar to the 24 June 2015 event. An even more dramatic example occurs on 27 August 2016 where THB spacecraft's lunar tail crossing includes a compressional wake but THC spacecraft's encounter a few hours later showed no evidence of the compressional wake.

In contrast, both observations and simulations provide support for the notion that the rarefaction wake is a semipermanent feature of the lunar tail and is present in most if not all regions around the tail. This contrast ties with the fact that the rarefaction wake diverts the flow toward the tail which is needed to refill the density cavity in the tail. On the other hand, it is hard to imagine the need for a semipermanent compressional wake given its tendency to divert the flow away from the tail. The time-dependent nature of this wake is more likely tied to the dynamics of the central tail region and remains to be understood in more detail in the future. It should also be noted that solar wind interaction with lunar crustal magnetic fields results in magnetic field and density enhancements (e.g., Fatemi et al., 2014) that are on the fast magnetosonic mode. As such, not all the observed density and magnetic field enhancements are associated with the compressional wake.

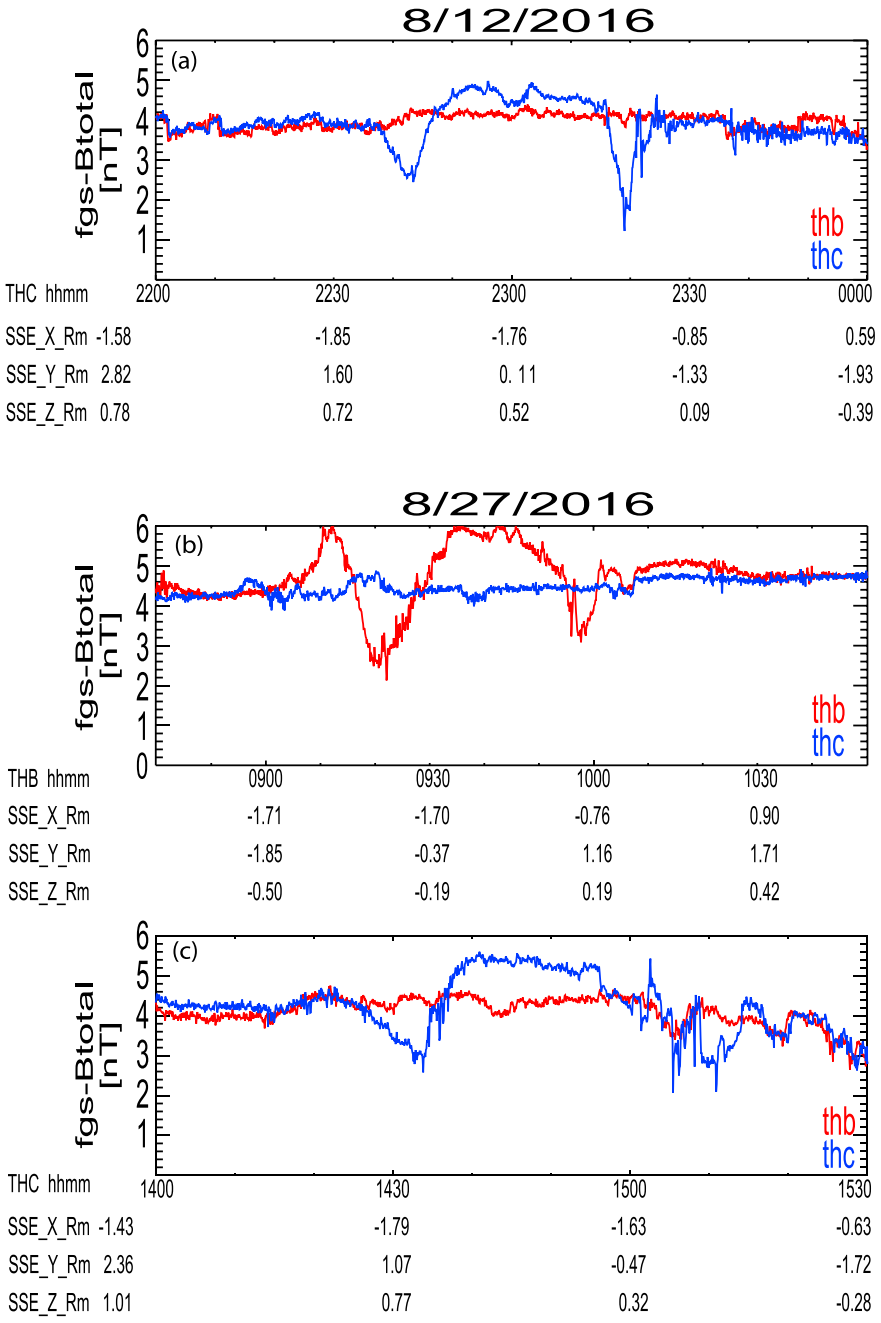

Figure 15. THB and THC observations of lunar tail on two crossings without the compressional wake on (a) 12 and (b, c) 27 August 2016.

Acknowledgments
Work for this project was supported by NASA grant NNX17A126G. ARTEMIS summary plots can be accessed from the THEMIS mission website (http://themis.ssl.berkeley.edu/index.shtml). ARTEMIS data can be accessed and analyzed using the SPEDAS (the Space Physics Environment Data Analysis Software) framework that can be downloaded from the THEMIS mission website. Simulation data are available at NASA PDS: Planetary Plasma Interactions node (https://pds-ppi.igpp.ucla.edu/).

References

Angelopoulos, V. (2008). The THEMIS mission. *Space Science Reviews*, *141*(1-4), 5–34. https://doi.org/10.1007/s11214-008-9336-1

Angelopoulos, V. (2011). The ARTEMIS mission. *Space Science Reviews*, *165*(1-4), 3–25. https://doi.org/10.1007/s11214-010-9687-2

Angelopoulos, V., Cruce, P., Drozdov, A., Grimes, E. W., Hatzigeorgiu, N., King, D. A., et al. (2019). The Space Physics Environment Data Analysis System (SPEDAS). *Space Science Reviews*, *215*(1), 9. https://doi.org/10.1007/s11214-018-0576-4

Clack, D., Kasper, J. C., Lazarus, A. J., Steinberg, J. T., & Farrell, W. M. (2004). Wind observations of extreme ion temperature anisotropies in the lunar wake. *Geophysical Research Letters*, *31*, L06812. https://doi.org/10.1029/2003GL018298

Colburn, D. S., Currie, R. G., Mihalov, J. D., & Sonett, C. P. (1967). Diamagnetic solar-wind cavity discovered behind Moon. *Science*, *158*(3804), 1040–1042. https://doi.org/10.1126/science.158.3804.1040

Colburn, D. S., Mihalov, J. D., & Sonett, C. P. (1971). Magnetic observations of the lunar cavity. *Journal of Geophysical Research*, *76*(13), 2940–2957. https://doi.org/10.1029/JA076i013p02940

Denavit, J. (1979). Collisionless plasma expansion into a vacuum. *Physics of Fluids*, *22*(7), 1384–1392. https://doi.org/10.1063/1.862751

Dhanya, M. B., Bhardwaj, A., Futaana, Y., Fatemi, S., Holmström, M., Barabash, S., et al. (2013). Proton entry into the near-lunar plasma wake for magnetic field aligned flow. *Geophysical Research Letters*, *40*, 2913–2917. https://doi.org/10.1002/grl.50617

Fatemi, S., Holmström, M., Futaana, Y., Barabash, S., & Lue, C. (2013). The lunar wake current systems. *Geophysical Research Letters*, *40*, 17–21. https://doi.org/10.1029/2012GL054635

Fatemi, S., Holmström, M., Futaana, Y., Lue, C., Collier, M. R., Barabash, S., & Stenberg, G. (2014). Effects of protons reflected by lunar crustal magnetic fields on the global lunar plasma environment. *Journal of Geophysical Research: Space Physics*, *119*, 6095–6105. https://doi.org/10.1002/2014JA019900

Halekas, J. S., Bale, S. D., Mitchell, D. L., & Lin, R. P. (2005). Electrons and magnetic fields in the lunar plasma wake. *Journal of Geophysical Research*, *110*, A07222. https://doi.org/10.1029/2004JA010991

Holmström, M., Fatemi, S., Futaana, Y., & Nilsson, H. (2012). The interaction between the moon and the solar wind. *Earth, Planets and Space*, *64*, 237–245. https://doi.org/10.5047/eps.2011.06.040

Lyon, E. F., Bridge, H. S., & Binsack, J. H. (1967). Explorer 35 plasma measurements in the vicinity of the Moon. *Journal of Geophysical Research*, *72*(23), 6113–6117. https://doi.org/10.1029/JZ072i023p06113

McFadden, J. P., Carlson, C. W., Larson, D., Bonnell, J., Mozer, F., Angelopoulos, V., et al. (2008). THEMIS ESA first science results and performance issues. *Space Science Reviews*, *141*(1-4), 477–508. https://doi.org/10.1007/s11214-008-9433-1

McFadden, J. P., Carlson, C. W., Larson, D., Ludlam, M., Abiad, R., Elliott, B., et al. (2008). The THEMIS ESA plasma instrument and in-flight calibration. *Space Science Reviews*, *141*(1-4), 277–302. https://doi.org/10.1007/s11214-008-9440-2

Michel, F. C. (1968). Magnetic field structure behind the moon. *Journal of Geophysical Research*, *73*(5), 1533–1542. https://doi.org/10.1029/JA073i005p01533

Ness, N. F., Behannon, K. W., Taylor, H. E., & Whang, Y. C. (1968). Perturbations of the interplanetary magnetic field by the lunar wake. *Journal of Geophysical Research*, *73*(11), 3421–3440. https://doi.org/10.1029/JA073i011p03421

Nishino, M. N., Fujimoto, M., Saito, Y., Tsunakawa, H., Kasahara, Y., Kawamura, M., et al. (2013). Type-II entry of solar wind protons into the lunar wake: Effects of magnetic connection to the night-side surface. *Planetary and Space Science*, *87*, 106–114. https://doi.org/10.1016/j.pss.2013.08.017

Ogilvie, K. W., Steinberg, J. T., Fitzenreiter, R. J., Owen, C. J., Lazarus, A. J., Farrell, W. M., & Torbert, R. B. (1996). Observations of the lunar plasma wake from the WIND spacecraft on December 27, 1994. *Geophysical Research Letters*, *23*(10), 1255–1258. https://doi.org/10.1029/96GL01069

Omidi, N., Collinson, G., & Sibeck, D. (2017). Structure and properties of the foreshock at Venus. *Journal of Geophysical Research: Space Physics*, *122*, 10,275–10,286. https://doi.org/10.1002/2017JA024180

Omidi, N., Tokar, R. L., Averkamp, T., Gurnett, D. A., Kurth, W. S., & Wang, Z. (2012). Flow stagnation at Enceladus: The effects of neutral gas and charged dust. *Geophysical Research Letters*, *117*, A06230. https://doi.org/10.1029/2011JA017488

Owen, C. J., Lepping, R. P., Ogilvie, K. W., Slavin, J. A., Farrell, W. M., & Byrnes, J. B. (1996). The lunar wake at 6.8 RL: WIND magnetic field observations. *Geophysical Research Letters*, *23*(10), 1263–1266. https://doi.org/10.1029/96GL01354

Samir, U., Wright, K. H. Jr., & Stone, N. H. (1983). The expansion of a plasma into a vacuum: Basic phenomena and processes and applications to space plasma physics. *Reviews of Geophysics*, *21*(7), 1631–1646. https://doi.org/10.1029/RG021i007p01631

Sibeck, D. G., Angelopoulos, V., Brain, D. A., Delory, G. T., Eastwood, J. P., Farrell, W. M., et al. (2011). ARTEMIS science objectives. *Space Science Reviews*, *165*(1–4), 59–91. https://doi.org/10.1007/s11214-011-9777-9

Sonett, C. P. (1982). Electromagnetic induction in the moon. *Reviews of Geophysics*, *20*(3), 411–455. https://doi.org/10.1029/RG020i003p00411

Wang, Y. C., Muller, J., Ip, W. H., & Motschmann, U. (2011). A 3D hybrid simulation study of the electromagnetic field distributions in the lunar wake. *Icarus*, *216*(2), 415–425. https://doi.org/10.1016/j.icarus.2011.09.021

Whang, Y. C. (1968). Theoretical study of the magnetic field in the lunar wake. *Physics of Fluids*, *11*(8), 1713. https://doi.org/10.1063/1.1692185

Whang, Y. C., & Ness, N. F. (1970). Observations and interpretation of the lunar Mach cone. *Journal of Geophysical Research*, *75*(31), 6002–6010. https://doi.org/10.1029/JA075i031p06002

Xie, L. H., Li, L., Zhang, Y. T., & de Zeeuw, D. L. (2012). Three-dimensional MHD simulation of the lunar wake. *Science China Earth Sciences*, *56*(2), 330–338. https://doi.org/10.1007/s11430-012-4383-6

Zhang, H., Khurana, K. K., Kivelson, M. G., Angelopoulos, V., Wan, W. X., Liu, L. B., et al. (2014). Three-dimensional lunar wake reconstructed from ARTEMIS data. *Journal of Geophysical Research: Space Physics*, *119*, 5220–5243. https://doi.org/10.1002/2014JA020111

Zhang, H., Khurana, K. K., Kivelson, M. G., Fatemi, S., Holmström, M., Angelopoulos, V., et al. (2016). Alfvén wings in the lunar wake: The role of pressure gradients. *Journal of Geophysical Research: Space Physics*, *121*, 10,698–10,711. https://doi.org/10.1002/2016JA022360